



**HAL**  
open science

# Mountain Waves Produced by a Stratified Boundary Layer Flow. Part I: Hydrostatic Case

François Lott, Bruno Deremble, Clément Soufflet

► **To cite this version:**

François Lott, Bruno Deremble, Clément Soufflet. Mountain Waves Produced by a Stratified Boundary Layer Flow. Part I: Hydrostatic Case. *Journal of the Atmospheric Sciences*, 2020, 77 (5), pp.1683-1697. 10.1175/JAS-D-19-0257.1 . hal-02998000

**HAL Id: hal-02998000**

**<https://hal.sorbonne-universite.fr/hal-02998000v1>**

Submitted on 10 Nov 2020

**HAL** is a multi-disciplinary open access archive for the deposit and dissemination of scientific research documents, whether they are published or not. The documents may come from teaching and research institutions in France or abroad, or from public or private research centers.

L'archive ouverte pluridisciplinaire **HAL**, est destinée au dépôt et à la diffusion de documents scientifiques de niveau recherche, publiés ou non, émanant des établissements d'enseignement et de recherche français ou étrangers, des laboratoires publics ou privés.

# 2 **Mountain waves produced by a stratified boundary** 3 **layer flow. Part I: Hydrostatic case.**

4 François Lott<sup>1</sup>, Bruno Deremble, and Clément Soufflet

5 *Laboratoire de Météorologie Dynamique, Ecole Normale Supérieure, PSL Research Institute, 24*  
6 *rue Lhomond, 75231 Paris France*

## 7 **Abstract**

8 An hydrostatic theory for mountain waves with a boundary layer of constant eddy viscosity is  
9 presented. It predicts that dissipation impacts the dynamics over an inner layer which depth is  
10 controlled by the inner layer scale  $\delta$  of viscous critical level theory. The theory applies when the  
11 mountain height is smaller or near  $\delta$  and is validated with a fully nonlinear model. In this case the  
12 pressure drag and the waves Reynolds stress can be predicted by inviscid theory, if one takes for  
13 the incident wind its value around the inner layer scale. In contrast with the inviscid theory and  
14 for small mountains the wave drag is compensated by an acceleration of the flow in the inner layer  
15 rather than of the solid earth. Still for small mountains and when stability increases, the emitted  
16 waves have smaller vertical scale and are more dissipated when traveling through the inner layer:  
17 a fraction of the wave drag is deposited around the top of the inner layer before reaching the outer  
18 regions. When the mountain height becomes comparable to the inner layer scale non-separated  
19 upstream blocking and downslope winds develop. Theory and model show that (i) the downslope  
20 winds penetrate well into the inner layer, (ii) upstream blocking and downslope winds are favored  
21 when the static stability is strong and (iii) are not associated with upper level wave breaking.

---

<sup>1</sup>Corresponding author: flott@lmd.ens.fr

## 1. Introduction

The impact of small to medium scale mountains on the atmospheric dynamics has been intensively studied over the last 50 years by two quite distinct communities. One community is studying how mountains modify the turbulent boundary layer (Jackson and Hunt, 1975), an issue that is central in the context of wind resource modeling (Ayotte, 2008) or dune formation (Charru et al., 2012). The associated theories form the basis of subgrid scale orography parameterizations, where the enhancement of turbulence caused by mountains is modeled by increasing the terrain roughness length (Wood and Mason, 1993). Wood et al. (2001) used fully nonlinear simulations to extend the theory and improve the estimate of the depth over which the mountain drag is deposited. These parameterizations are used for mountains with horizontal scales smaller than 5000 m (Beljaars et al., 2004). At these scales one can expect that the horizontal scale of the mountains,  $L$ , is such that the advective time scale,  $L/u_0$  is smaller than the inverse of the buoyancy frequency  $N^{-1}$ . This ensures that the flow behaves according to neutral flow dynamics.

The second community is more focused on mountain dynamical meteorology. It studies the onset of downslope winds, foehn, and trapped waves using theories and models where internal gravity waves control the dynamics, and where the boundary layer is often neglected. The relevance of the approach is illustrated by Sheridan et al. (2017) where a near linear mountain wave model permits to interpret wind perturbations due to mountain wave events over the UK. The associated theory is extremely vast in itself (Durrán, 1990). Among other things, this theory has been used to predict realistic partitions between upper level and lower level wave drag and orographic blocking, which are concepts that are used in parameterizations of subgrid scale orography with horizontal scales  $L > 5000$  m (Lott and Miller, 1997). Note that this type of parameterization is still used in atmospheric models, and even in the models with horizontal resolution that resolve these scales (Sandu et al., 2015; Pithan et al., 2016). In fact, it is not so clear whether there is a critical mountain size ( $L = 5000$  m) below which the flow would only impact the boundary layer and above which the flow would only impact the waves. We actually believe that this criteria is quite adhoc and should depend on the nature of the flow.

Because boundary layer dynamics is highly controlled by the inviscid dynamics aloft, and because in mountain meteorology the wave forcing is embedded into the boundary layer, it soon appeared that the two communities should make some effort to integrate results from the other community. It is in this context that Hunt et al. (1988) and Belcher and Wood (1996) included stratification and gravity waves in boundary layer theories over mountain. Belcher and Wood (1996) showed that when the Froude number  $F = u_0/NL$  is smaller than 1, the mountain drag is due to mountain gravity waves (rather than boundary layer effect) and is well predicted by linear gravity mountain wave theory. This result actually depends on the height at which one chooses

57 the reference velocity  $u_0$  and reference Brunt Vaisala frequency  $N$ . As we shall see, in the absence  
58 of background wind curvature, the relevant altitude to compute these quantities is that of the inner  
59 layer, which is the altitude where disturbance advection by the background wind is balanced by  
60 dissipation. Still in this context but in the mountain meteorology community, studies using nu-  
61 merical model show that the boundary layer drag reduces downslope windstorms and mountain  
62 waves (Richard et al., 1989; Olafsson and Bougeault, 1997). More recent observations show that  
63 the atmospheric boundary layer can absorb downward propagating waves and weaken trapped lee  
64 waves (Smith et al., 2002; Jiang et al., 2006). These last results have motivated a series of theo-  
65 retical studies on the interaction between the boundary layer and mountain waves. All so far use  
66 crude parameterizations of the boundary layer: Smith et al. (2006) uses a bulk boundary layer  
67 model, Lott (2007) uses constant eddy viscosity, and Lott (2016) uses linear drags (Newtonian  
68 cooling and Rayleigh drag).

69 Despite these simplifications, these studies reproduce the increase in trapped waves absorption  
70 when stability increases, insisting on cases where the incident wind is weak near the ground. This  
71 near surface critical level situation, a situation that was little studied because it poses fundamental  
72 problems in the inviscid mountain wave theory, was nevertheless found to produce interesting dy-  
73 namics. Near surface critical level favors downslope windstorms and Foehn (Lott, 2016; Damiens  
74 et al., 2018) and permits to establish a bridge between trapped lee waves and Kelvin-Helmholtz  
75 instabilities (Lott, 2016; Soufflet et al., 2019). Interestingly, the critical level mechanism that is a  
76 priori a dissipative mechanism turned out to be extremely active dynamically.

77 To summarize, there are two descriptions of the interaction between boundary layers and moun-  
78 tain waves: on the one hand boundary layer studies tell that the pressure drag is controlled by  
79 the mountain wave dynamics outside of the boundary layer, but imposes very simplified dynamics  
80 outside of it (Belcher and Wood, 1996). And on the other hand, "mountain wave" studies that give  
81 great attention to the potential impact of a boundary layer on mountain waves but that use very  
82 simplified boundary layer representation (Smith et al., 2006). We actually believe that there is still  
83 room to develop a theory where the boundary layer and the mountain wave field fully interact in  
84 a comprehensive way. We see at least three reasons for this. The first is that in mountain wave  
85 theory, the gravity wave (GW) field is controlled by the low level flow amplitude, and it is not  
86 obvious to tell at which (or over which) altitude it should be measured in the absence of strong  
87 wind curvatures. Second, we know that the inviscid dynamics potentially produces downslope  
88 winds in the stratified case and it could be interesting to test if they extend down to the surface and  
89 well into the inner layer. Last, we know that the pressure drag is controlled by the wave drag in the  
90 stable case, but we do not know if a fraction of the wave drag could and should be deposited into

91 the inner layer rather than being radiated away. This issue could have important consequences for  
92 the formulation of parameterizations.

93 The purpose of the present paper is to answer these questions in the reference case where the  
94 boundary layer is parameterized via a constant kinematic eddy viscosity  $\nu$ . This case has the  
95 unique merit that, while the Couette profile with constant shear  $u_{0z}$  is an exact solution, we can  
96 handle the interactions with topography using the stratified viscous solutions derived by Hazel  
97 (1967) and Baldwin and Roberts (1970). However, a consequence of using uniform wind shear is  
98 that the "boundary layer depth" of the incident flow is infinite, it is therefore totally distinct from  
99 the "inner layer depth" over which the waves are affected by dissipation and that scales as

$$\delta = \left( \frac{\nu L}{u_{0z}} \right)^{\frac{1}{3}}. \quad (1)$$

100 These simplifications of uniform viscosity and background shear were made in the literature of  
101 the late 50's by Benjamin (1959) and Smith (1973) in the context of flows over water waves and  
102 dunes respectively. Since then, we are well aware that such a "laminar" approach is an extreme  
103 idealization. A reason is that boundary layer dynamics tends to produce winds with strong shears  
104 near aloft the surface but that vary much more slowly at higher altitudes (the associated curvatures  
105 defining the "boundary layer depth" quite precisely). To defend our choice nevertheless, we can  
106 recall that in the atmosphere the low level wind shears are not only due to the boundary layer:  
107 they are also related to the large scale dynamics. This has been shown for instance in experiments  
108 done by Sheridan et al. (2007) and Doyle et al. (2011), where they observe strong shears over  
109 few kilometers above the ground. This being said, we will have to keep in mind that models with  
110 constant eddy viscosity probably overstate the significance of the low level shear stresses on the  
111 waves and pressure drag (Sykes, 1978).

112 The plan of the paper is as follows. In section 2 we derive the theory in the hydrostatic case.  
113 In section 3 we discuss the pressure drag and wave momentum fluxes it predicts. In section 4  
114 we analyze the onset of downslope winds. As our theory is linear except for the lower boundary  
115 condition, our results are checked against fully nonlinear simulations in Section 5. In section 6, we  
116 discuss further the significance of works on boundary layer using constant eddy viscosity. We also  
117 discuss in this section how our results could be useful to understand the dynamics in more realistic  
118 cases. In Appendix A, we detail some aspects of the theory, and in Appendix B we provide details  
119 on the numerical implementation of the model.

## 120 2. Theory

### 121 a. Basic equations

122 We consider a background flow solution of the viscous equations,

$$u_0(z) = u_{0z}z; \rho_0(z) = \rho_r + \rho_{0z}z, \quad (2)$$

123 where the wind shear  $u_{0z}$  and stratification  $\rho_{0z}$  are both constant, and that is incident on a Gaussian  
124 ridge of characteristic length  $L$  and maximum height  $H$ :

$$h(x) = He^{-x^2/(2L^2)}. \quad (3)$$

125 Following quite conventional approaches (Beljaars et al., 1987; Belcher and Wood, 1996), we  
126 consider obstacles of small slope and use linear equations. To characterize the factors that control  
127 the dynamics we also normalize the response by introducing the "outer" scaling:

$$(x, z) = L(\bar{x}, \bar{z}), \quad (u', w') = u_{0z}L(\bar{u}, \bar{w}), \quad (p', b') = (\rho_r u_{0z}^2 L^2 \bar{p}, u_{0z}^2 L \bar{b}) \quad (4)$$

128 where  $u'$  and  $w'$  are the horizontal and vertical wind disturbances whereas  $b'$  is the buoyancy  
129 disturbance. With this scaling, and making the conventional "Prandtl" approximation that the  
130 vertical derivatives dominate the viscous terms, the 2D Boussinesq hydrostatic linear equations  
131 write:

$$\bar{z}\partial_{\bar{x}}\bar{u} + \bar{w} = -\partial_{\bar{x}}\bar{p} + \bar{\nu}\partial_{\bar{z}}^2\bar{u}, \quad (5a)$$

$$0 = -\partial_{\bar{z}}\bar{p} + \bar{b} \quad (5b)$$

$$\bar{z}\partial_{\bar{x}}\bar{b} + J\bar{w} = P^{-1}\bar{\nu}\partial_{\bar{z}}^2\bar{b}, \quad (5c)$$

$$\partial_{\bar{x}}\bar{u} + \partial_{\bar{z}}\bar{w} = 0. \quad (5d)$$

135 with no-slip boundary conditions:

$$\bar{h}(\bar{x}) + \bar{u}(\bar{x}, \bar{h}) = 0, \quad \bar{w}(\bar{x}, \bar{h}) = 0, \quad \text{and } J\bar{h}(\bar{x}) + \bar{b}(\bar{x}, \bar{h}) = 0 \text{ at } \bar{h} = Se^{-\bar{x}^2/2}. \quad (6)$$

136 In Eqs. (5)-(6),

$$J = -\frac{g\rho_{0z}}{\rho_r u_{0z}^2}, \quad P = \frac{\nu}{\kappa}, \quad S = \frac{H}{L}, \quad \text{and } \bar{\nu} = \frac{\nu}{u_{0z}L^2} \quad (7)$$

137 are a Richardson number, a Prandtl number, a slope parameter and an inverse Reynolds number  
138 respectively.

139 To help establish where the waves are produced and where they are dissipated we next derive  
140 from Eqs. 5 a wave-action budget. As this is not often done in mountain waves literature we recall  
141 that the interest is to define a quantity  $A$  that is quadratic (to measure the wave amplitude locally)

142 and conservative in the adiabatic frictionless case. For action we chose the pseudo-momentum,  
 143 because its vertical flux,  $F^z$  is closely related to the mountain wave Reynolds stress<sup>2</sup> (see further  
 144 discussions in Durran (1995) and Lott (1998)). Although the exact form of the wave action is  
 145 rigorously derived when starting from Hamiltonian dynamics (Scinocca and Shepherd, 1992), we  
 146 can directly use the the formula for the pseudo-momentum  $A$  derived in this paper, and derive a  
 147 budget that includes dissipation by doing the formal operation:

$$\frac{\bar{b}}{J} \partial_{\bar{z}} (\text{Eq. 5a}) + \frac{\bar{u}_{\bar{z}}}{J} (\text{Eq. 5c}). \quad (8)$$

148 After few integrations by parts one obtains,

$$\frac{\partial}{\partial \bar{x}} \underbrace{\left( \bar{z} \underbrace{\frac{\partial_{\bar{z}} \bar{u}}{J} \bar{b} + \frac{\bar{b}^2}{2J} + \frac{\bar{u}^2}{2}}_A \right)}_{F^x} + \frac{\partial}{\partial \bar{z}} \underbrace{\bar{u} \bar{w}}_{F^z} = \underbrace{\bar{v} \frac{\bar{b}}{J} \partial_{\bar{z}}^2 \partial_{\bar{z}} \bar{u} + P^{-1} \bar{v} \partial_{\bar{z}} \bar{u} \partial_{\bar{z}}^2 \bar{b}}_Q, \quad (9)$$

149 where  $F^x$  and  $F^z$  the horizontal and vertical components of the pseudo-momentum flux, and where  
 150  $Q$  is the production/destruction of action by dissipative processes. Note that  $F^x$  includes the hor-  
 151 izontal advection of action by the background flow  $\bar{z}A$ . As we search inflow solutions that are  
 152 linear, we next express them in terms of Fourier transform,

$$\bar{w}(\bar{x}, \bar{z}) = \int_{-\infty}^{+\infty} \bar{w}(\bar{k}, \bar{z}) e^{i\bar{k}\bar{x}} d\bar{k}, \text{ where } \bar{w}(\bar{k}, \bar{z}) = \frac{1}{2\pi} \int_{-\infty}^{+\infty} \bar{w}(\bar{x}, \bar{z}) e^{-i\bar{k}\bar{x}} d\bar{x}, \quad (10)$$

153 which transforms Eqs. 5 into:

$$i\bar{k}\bar{z}\bar{u} + \bar{w} = -i\bar{k}\bar{p} + \bar{v}\partial_{\bar{z}}^2 \bar{u}, \quad (11a)$$

$$i\bar{k}\bar{z}\bar{b} + J\bar{w} = P^{-1}\bar{v}\partial_{\bar{z}}^2 \bar{b}, \quad (11b)$$

$$\bar{b} = \partial_{\bar{z}} \bar{p}, \quad i\bar{k}\bar{u} + \partial_{\bar{z}} \bar{w} = 0. \quad (11c)$$

## 157 *b. Solutions*

158 For high Reynolds number  $\bar{v} \ll 1$ , the dynamics is inviscid at leading order. Each harmonics  
 159 satisfy Eqs. 11 with  $\bar{v} = 0$ , which results in  $\bar{w}$  satisfying,

$$\bar{w}_{\bar{z}\bar{z}} + \frac{J}{\bar{z}^2} \bar{w} = 0. \quad (12)$$

160 Such equation has two solutions (Booker and Bretherton, 1967):

$$\bar{z}^{\frac{1}{2} \pm i\mu}, \text{ where } \mu = \sqrt{J - \frac{1}{4}}. \quad (13)$$

---

<sup>2</sup>It is actually interesting to recall that the seminal paper on wave mean flow interaction by Eliassen and Palm (1961) was about mountain waves.

161 When  $\bar{k} > 0$  and  $J > 0.25$ , only the solution

$$\bar{\mathbf{w}}_I(\bar{k}, \bar{z}) = \bar{z}^{1/2+i\mu}, \quad (14)$$

162 corresponds to a gravity wave propagating upward. The cases with  $\bar{k} < 0$  are treated by com-  
 163 plex conjugation and will not be discussed further. The cases with  $J < 0.25$  are degenerated in  
 164 the hydrostatic approximation because the direction of vertical propagation can not be used to  
 165 distinguish between the two solutions in (13). This difficulty, which forbids to treat the weakly  
 166 stratified cases (i.e., here when  $J < 1/4$ ), will be resolved in a future non-hydrostatic treatment of  
 167 the inviscid solution.

168 To solve the inner layer we introduce the scaling,

$$\bar{z} = \bar{\delta}\tilde{z}, (\bar{\mathbf{u}}, \bar{\mathbf{w}}) = (\tilde{\mathbf{u}}, \bar{\delta}\tilde{k}\tilde{\mathbf{w}}), (\bar{p}, \bar{b}) = (\bar{\delta}\tilde{p}, \tilde{b}) \text{ where } \bar{\delta} = \left(\frac{\bar{v}}{\bar{k}}\right)^{\frac{1}{3}}. \quad (15)$$

169 At leading order, it transforms the full set of non dimensional Eqs. 5 into the sixth-order set:

$$\partial_{\tilde{z}}^2 \tilde{\mathbf{u}} = i\tilde{z}\tilde{\mathbf{u}} + \tilde{\mathbf{w}} + i\tilde{\mathbf{p}}, \quad (16a)$$

$$\partial_{\tilde{z}}^2 \tilde{\mathbf{b}} = P(i\tilde{z}\tilde{\mathbf{b}} + J\tilde{\mathbf{w}}), \quad (16b)$$

$$\partial_{\tilde{z}}\tilde{\mathbf{w}} = -i\tilde{\mathbf{u}}, \partial_{\tilde{z}}\tilde{\mathbf{p}} = \tilde{\mathbf{b}}. \quad (16c)$$

172 This set of Eqs. can be reduced to one single equation for  $\tilde{\mathbf{w}}$ ,

$$(\partial_{\tilde{z}}^2 - iP\tilde{z})(\partial_{\tilde{z}}^2 - i\tilde{z})\partial_{\tilde{z}}^2 \tilde{\mathbf{w}} = JP\tilde{\mathbf{w}}, \quad (17)$$

173 that has six independent solutions. Hazel (1967) and Baldwin and Roberts (1970) have found their  
 174 asymptotic form when  $\tilde{z} \rightarrow \infty$ . Two grow exponentially as  $\tilde{z} \rightarrow \infty$  and cannot be used (Van Duin  
 175 and Kelder, 1986), the four that remain have asymptotic forms:

$$\tilde{\mathbf{w}}_1 \underset{\tilde{z} \rightarrow \infty}{\approx} \tilde{z}^{1/2-i\mu}, \tilde{\mathbf{w}}_2 \underset{\tilde{z} \rightarrow \infty}{\approx} \tilde{z}^{1/2+i\mu}, \tilde{\mathbf{w}}_3 \underset{\tilde{z} \rightarrow \infty}{\approx} \tilde{z}^{-5/4} e^{-\frac{2\sqrt{i}}{3}\tilde{z}^{3/2}}, \tilde{\mathbf{w}}_4 \underset{\tilde{z} \rightarrow \infty}{\approx} \tilde{z}^{-9/4} e^{-\frac{2\sqrt{iP}}{3}\tilde{z}^{3/2}}. \quad (18)$$

176 In Lott (2007), these four solutions are evaluated over the entire domain  $0 < \tilde{z} < \infty$ , i.e. by using the  
 177 asymptotic forms (18) above  $\tilde{z} = 5$  and integrating down Eq. (17) from  $\tilde{z} = 5$  to  $\tilde{z} = 0$  with a Runge  
 178 Kutta algorithm. We will essentially proceed like this here (some serious convergence issues are  
 179 discussed in the appendix). We then notice that the inner function  $\tilde{\mathbf{w}}_2$  matches the upward inviscid  
 180 solution (14) and that  $\tilde{\mathbf{w}}_3$  and  $\tilde{\mathbf{w}}_4$  decay exponentially fast with altitude, which permit to tell that all  
 181 the combinations of  $\tilde{\mathbf{w}}_2$ ,  $\tilde{\mathbf{w}}_3$  and  $\tilde{\mathbf{w}}_4$  are uniform solutions that can match  $\bar{\mathbf{w}}_I$ . We therefore search  
 182 a uniform approximation of the vertical velocity under the form,

$$\bar{\mathbf{w}}(\bar{k}, \bar{z}) = \bar{k}\bar{\delta}(k) \left[ f_2(\bar{k})\tilde{\mathbf{w}}_2(\bar{z}/\bar{\delta}(\bar{k})) + f_3(\bar{k})\tilde{\mathbf{w}}_3(\bar{z}/\bar{\delta}(\bar{k})) + f_4(\bar{k})\tilde{\mathbf{w}}_4(\bar{z}/\bar{\delta}(\bar{k})) \right] \quad (19)$$



183 where all fields are expressed using outer variables, and with similar expression for  $\bar{\mathbf{u}}$  and  $\bar{\mathbf{b}}$  de-  
 184 duced from (11). To evaluate the unknown functions  $f_2$ ,  $f_3$  and  $f_4$ , we write the boundary condi-  
 185 tions:

$$\bar{w}(\bar{x}, \bar{h}) \approx \int_{-\infty}^{+\infty} \bar{k} \bar{\delta}(\bar{k}) (f_2(\bar{k}) \tilde{\mathbf{w}}_2(\tilde{h}) + f_3(\bar{k}) \tilde{\mathbf{w}}_3(\tilde{h}) + f_4(\bar{k}) \tilde{\mathbf{w}}_4(\tilde{h})) e^{i\bar{k}\bar{x}} d\bar{k} = 0, \quad (20a)$$

$$\bar{u}(\bar{x}, \bar{h}) \approx \int_{-\infty}^{+\infty} (f_2(\bar{k}) \tilde{\mathbf{u}}_2(\tilde{h}) + f_3(\bar{k}) \tilde{\mathbf{u}}_3(\tilde{h}) + f_4(\bar{k}) \tilde{\mathbf{u}}_4(\tilde{h})) e^{i\bar{k}\bar{x}} d\bar{k} = -\bar{h}(\bar{x}), \quad (20b)$$

$$\bar{b}(\bar{x}, \bar{h}) \approx \int_{-\infty}^{+\infty} (f_2(\bar{k}) \tilde{\mathbf{b}}_2(\tilde{h}) + f_3(\bar{k}) \tilde{\mathbf{b}}_3(\tilde{h}) + f_4(\bar{k}) \tilde{\mathbf{b}}_4(\tilde{h})) e^{i\bar{k}\bar{x}} d\bar{k} = -J\bar{h}(\bar{x}), \quad (20c)$$

188 where  $\tilde{h}(\bar{x}, \bar{k}) = \bar{h}(\bar{x}) / \bar{\delta}(\bar{k})$ . Once discretized in the horizontal and spectral domain, the set of  
 189 equations (20) corresponds to three linear equations for  $f_2(\bar{k})$ ,  $f_3(\bar{k})$  and  $f_4(\bar{k})$  that can be inverted  
 190 with conventional matrix inversion routines (see appendix for more details on the numerical treat-  
 191 ment).

### 192 3. Mountain wave fields and drags

193 We plot in figure 1 the flow response when the inverse Reynolds number  $\bar{\nu} = 0.001$ , the slope  
 194 parameter  $S = 0.01$ , the Richardson number  $J = 4$ , and the Prandtl number  $\text{Pr} = 0.5$ . This last  
 195 parameter will stay unchanged in the rest of the paper: we have found moderate sensitivity of  
 196 the upper wave fields to this parameter as long as its value stays around 1. In this setup, the  
 197 characteristic inner layer scale is that of the dominant harmonic  $\bar{k} = 1$ , i.e.  $\bar{\delta}(\bar{k} = 1) = \bar{\nu}^{1/3} = 0.1$ ,  
 198 which is also the nondimensional form of the inner layer scale in (1). The inner layer scale is  
 199 therefore much larger than the mountain slope.

200 The total wind at low level in Fig. 1a contours well the obstacle and the vertical velocity field  
 201 (Fig. 1b) highlight a system of well defined upward propagating gravity waves. We notice that  
 202 the stream function in Fig. 1c follows well the orography, up to at least the inner layer scale  
 203  $\bar{\delta}(1) = 0.1$ . For each altitudes below and around  $\bar{\delta}(1)$  the streamlines are displaced vertically over  
 204 distances that are near the mountain height  $S$ , and the vertical velocity when  $\bar{z} \approx \bar{\delta}$  should scale as  
 205  $\bar{w} \approx \frac{\bar{\delta}(1)}{2} S$  to follow the streamlines. We therefore propose that the wave amplitude corresponds  
 206 to the inviscid case when a uniform flow of amplitude  $\bar{\delta}(1)/2$  (the average of the incident wind  
 207 over the inner layer scale) is incident over a mountain of maximum height  $S$ . Far aloft and in the  
 208 sheared case, the vertical velocity should therefore scale as  $\bar{w} = 0 \left( \frac{\sqrt{\bar{z}\bar{\delta}(1)}}{2} S \right)$ , where the square  
 209 root corresponds to the  $\frac{1}{2}$  factor in the exponent of the inviscid solution (14). This qualitative  
 210 argument tells that the amplitude of  $\bar{w}$  should be around  $S\bar{\delta}(1)/2 = 5.10^{-4}$  at  $\bar{z} = 1$ , which is in  
 211 qualitative agreement with what is found in Fig. 1b.

212 We follow this line of qualitative reasoning and propose as predictor of the wave momentum  
 213 flux and mountain pressure drag,

$$\overline{u\overline{w}}(\overline{z}) = \int_{-\infty}^{+\infty} \overline{u}(\overline{x}, \overline{z}) \overline{w}(\overline{x}, \overline{z}) d\overline{x}, \quad Dr = - \int_{-\infty}^{+\infty} \overline{p}(\overline{x}, \overline{h}) \frac{\partial \overline{h}}{\partial \overline{x}} d\overline{x}, \quad (21)$$

214 the inviscid linear hydrostatic pressure drag produced by a uniform wind of intensity  $\overline{\delta}(1)/2$  inci-  
 215 dent on the orography given by  $\overline{h}(\overline{x})$  in (6), and which exact value is

$$-\frac{\overline{\delta}(1)}{2} \sqrt{JS^2} = -Dr_{GWP}. \quad (22)$$

216 Henceforth, we will refer to  $Dr_{GWP}$  as the gravity wave drag amplitude predictor. Figure 2 shows  
 217 that this predictor is a good estimate for the drag given by the theoretical model for a very large  
 218 range of  $J$  and slope  $S$ . We conclude that the pressure drag is well controlled by the inviscid GW  
 219 dynamics outside of the inner layer, the GWs being forced by the undulations of the inner layer  
 220 produced by the mountain. This picture where the inner layer forces the (inviscid) dynamics aloft,  
 221 and that the pressure drag is ultimately controlled by this inviscid dynamics follows the general  
 222 principle of boundary layer theories that pressure is approximately constant across the inner layer.

223 This predictor of the surface pressure drag is nevertheless misleading if we take it as a measure  
 224 of the effect of the mountain on the large-scale flow, as is generally done in mountain meteorology.  
 225 The reason is that, in a steady state, our waves are forced indirectly by the distortion of the inner  
 226 layer produced by the mountain rather than directly by the mountain as in the inviscid case. To  
 227 establish this, we return to Fig. 1d where we plotted the waves pseudomomentum flux vector. Aloft  
 228 the inner layer this flux clearly points down, as expected for mountain GWs propagating upward  
 229 (Durran, 1995; Lott, 1998), but within the inner layer, it points very strongly from the upstream  
 230 sector toward the downstream sector. This is to be contrasted with the inviscid case where this flux  
 231 goes through the surface and produces an exchange of momentum between the fluid and the solid  
 232 ground.

233 This result suggests that the acceleration that balances the gravity wave drag is not communi-  
 234 cated to the earth surface but rather to the inner layer. This last statement is confirmed in Fig. 3a  
 235 where we plot the wave stress as a function of altitude. The wave stress is null at the surface,  
 236 increases with altitude before reaching a constant value at altitudes above  $\overline{z} > 5\overline{\delta}(1)$  typically. As  
 237 is often the case for viscous boundary layers, the depth over which dissipation is significant seems  
 238 to be around 5 times the inner layer scale  $\overline{\delta}(1)$ , so we will systematically make the distinction  
 239 between the inner layer scale ( $\overline{\delta}(1)$ ) and the inner layer depth (around  $5\overline{\delta}(1)$ ). The flux emitted at  
 240 the top of the inner layer (above  $5\overline{\delta}(1)$ ) is around half the pressure drag, at least when when  $J \approx 1$ .  
 241 Such value stays comparable to the theoretical drag but suggests that substantial wave dissipation  
 242 occurs when the wave travels vertically through the inner layer (in our scenario where the waves

243 are forced around  $\bar{\delta}(1)$ ). This erosion of the pressure drag toward the gravity wave stress is even  
 244 more significant when  $J$  increases. This is again consistent with a qualitative argument: for large  
 245 values of  $J$ , the waves oscillate more rapidly in the vertical according to Eq. (14) and are more  
 246 affected by viscous dissipation. This difficulty in converting the pressure drag into a momentum  
 247 flux as stability increases makes that for  $J > 4$  typically, there is a minimum in  $\bar{u}\bar{w}$  in the middle  
 248 of the inner layer (between  $2\bar{\delta}(1)$  and  $5\bar{\delta}(1)$ ): part of the momentum given to the inner layer near  
 249 the surface is restored back around the top of the inner layer.

250 To understand what can replace the Reynolds stress to balance the pressure drag, it is important  
 251 to return to the initial Eliassen and Palm (1961)'s paper where it is shown that the momentum flux  
 252 is related to the pressure force exerted in the horizontal direction on an undulating surface. In the  
 253 linear stationary case, this relation is obtained by multiplying a momentum equation (Eq. 5a in our  
 254 case) by the vertical displacement of streamlines  $\bar{\eta}$  and after integration by part over  $\bar{x}$  we get

$$\bar{u}\bar{w} = -\overline{p\partial_x\bar{\eta}} - \bar{v}\left(\bar{\eta}\partial_z^2\bar{u}\right), \text{ where } \bar{z}\partial_x\bar{\eta} = \bar{w}. \quad (23)$$

255 In the inviscid case the pressure stress equals the Reynolds stress, but this is no longer true in  
 256 the viscous scenario where dissipation plays a non negligible role. To illustrate how dissipation  
 257 becomes significant for small slopes, we plot the two terms on the right hand side and their sum for  
 258 three values of  $J$  in Fig. 3b. After verification that the sum in Fig. 3b exactly equals the Reynolds  
 259 stresses in Fig. 3a, we see that Reynolds stress and the pressure drag only coincide well above  
 260 the boundary layer. Near the surface and in the lower part of the inner layer, the pressure drag is  
 261 almost entirely balanced by the viscous drag.

262 This erosion of the pressure drag toward the wave Reynolds stress is summarized in Fig. 4a  
 263 where we plot the Reynolds stress emitted in  $\bar{z} \rightarrow \infty$  normalized by the predictor  $Dr_{GWP}$ . As  
 264 already discussed, the emitted flux is half the predicted drag, but this result becomes sensitive to  
 265 the stability  $J$ : when  $J$  is large, the emitted flux almost vanishes. This erosion of the pressure drag  
 266 toward the Reynolds stress for large  $J$  is less pronounced if we consider the minimum values in  
 267 Fig. 4b. These minima are in general located in the middle of the inner layer (i.e. above  $\bar{z} = \bar{\delta}(1)$   
 268 and below  $5\bar{\delta}(1)$ ), (see Fig. 3a) such that for large  $J$  some GW deceleration should be applied  
 269 directly around the top of the boundary layer (which we locate at  $5\bar{\delta}(1)$ ).

#### 270 4. Non-separated blocking and downslope winds

271 To analyze what occurs in nonlinear situations we next consider cases where the slope  $S$  be-  
 272 comes comparable to the boundary layer scale  $\bar{\delta}(1)$ . As a first example, the simulation in Fig. 5  
 273 corresponds to that in Fig. 1 but with  $S = 0.15$  instead of  $S = 0.01$ . We readily notice that the  
 274 total wind (Fig. 5a) presents an downslope/upslope asymmetry that is almost absent in Fig. 1a.

275 The vertical velocity is around 30 times larger than in the small slope case, i.e. 3 times larger  
 276 than what should have been obtained if we applied a linear ratio of the slopes (Figs. 5b and 1b).  
 277 The asymmetry in the winds is also visible in the stream function in Fig. 5c, with a pronounced  
 278 descent on the lee side. Finally, the largest differences are maybe in the pseudo-momentum flux  
 279 vector in Fig. 5d. Now that the obstacle penetrates well into the boundary layer, there is a sub-  
 280 stantial pseudo-momentum flux across the surface. In opposition to the inviscid case (Lott, 1998)  
 281 we did not identify clear relations between this flux and the mountain drag, except that the total  
 282 flux across the surface is of the same order of magnitude as the mountain drag when the slope  
 283 approaches the inner layer scale.

284 To appreciate more systematically the changes occurring when the slope parameter increases  
 285 as a function of stability, we plot in Fig. 6 the vertical velocity fields for different values of  $S$   
 286 and  $J$ . The panels in the top row are for a slope that is small compared to the inner layer scale  
 287 ( $S = 0.02 < \bar{\delta}(1)$ ) and those in the bottom row for a slope that compares to it ( $S = 0.15 \approx \bar{\delta}(1)$ ).  
 288 The contour interval stays the same between all panels with given slope, consistent with the fact  
 289 that the kinematic boundary conditions are independent of  $J$  (see Eq. 6). Between the upper and  
 290 lower row where the slope changes, the contour interval changes with a factor proportional to the  
 291 slope ratio, i.e. following a linear relation. For the small slope cases when  $J$  increases (Figs. 6a,  
 292 6b, and 6c), one sees that the wave amplitude in the far field decreases with  $J$ . If we recall  
 293 that the vertical scale of variations of our solutions is inversely proportional to  $J$ , larger values  
 294 of  $J$  correspond to cases where the solutions oscillate more in the vertical direction, these plots  
 295 are therefore consistent with the interpretation that with large  $J$  the waves are more dissipated  
 296 when they travel through the inner layer. When the slope increases, a second interesting behavior  
 297 is worth noticing. When  $J = 1$  there are little differences between the patterns in Figs. 6a and  
 298 6d, which means that amplitudes varies linearly with  $S$  (remember that the contour interval varies  
 299 linearly with  $S$  between the upper and lower row). Again, we know since Lott (2016) and Damiens  
 300 et al. (2018) that this is also related to the vertical scale of the waves: strong nonlinear effects enter  
 301 the dynamics via the surface boundary condition and when the vertical wavelength at the top of  
 302 the obstacle compares to the vertical wavenumber, a criteria that corresponds to  $J > 1$ . As we see  
 303 in the following panels in Figs. 6e and 6f these nonlinear effects become substantial: for a given  
 304 slope the wave amplitude now increases when  $J$  increases. In addition to the enhanced emission due  
 305 to nonlinearities, it is also plausible that the wave dissipation through the inner layer is less intense  
 306 because the level of emission is located at a higher altitude than for smaller slopes. If we return  
 307 to the emitted momentum fluxes in Fig. 4, a consequence of these enhanced emission and reduced  
 308 dissipation when the slope increase and for large  $J$  is that the inviscid predictor of the momentum  
 309 flux  $Dr_{GWP}$  becomes more and more accurate (see the grey dotted line in Figs. 4a and 4b).

310 If we now return to the total winds in Fig. 7 we also see that for large slope and large  $J$ , the  
 311 winds along the upslope flank of the mountain become small compared to the downslope winds,  
 312 an asymmetry that increases with both  $S$  and  $J$ . More specifically, when  $J = 1$  (Fig. 7a) the flow  
 313 contours the obstacle: the flow is upward on the upwind side and downward on the downwind side  
 314 with little asymmetry in amplitudes, a behavior that is little affected by the increase in the slope  
 315 in Fig. 7d. When  $J$  increase and still for small slope in Figs. 7b and 7c some upwind/downwind  
 316 asymmetry starts to occur but stays limited: there is still substantial ascent on the upstream side  
 317 of the obstacle. This ascent is actually not confined to the lower layers but extends up to at least  
 318 twice the mountain slope. When the slope is larger (Figs. 7e and 7f), the upwind ascent is much  
 319 smaller than the downwind descent. The downwind descent extends well along the downwind  
 320 slope whereas along the upwind slope the total wind is very small. We call this situation a "non-  
 321 separated" blocking because it is produced by linear inflow dynamics.

322 To quantify the dependence on  $S$  and  $J$  more systematically in terms of upstream blocking and  
 323 downslope winds, we plot in Fig. 8 the ratio between the wind amplitude along the downwind  
 324 slope and the upwind slope of the ridge defined as

$$\underbrace{\text{Max}}_{\bar{z} < \frac{2\bar{h}}{3}, 0 < \bar{x} < 2} \sqrt{(\bar{z} + \bar{u})^2 + \bar{w}^2} \bigg/ \underbrace{\text{Max}}_{\bar{z} < \frac{2\bar{h}}{3}, -2 < \bar{x} < 0} \sqrt{(\bar{z} + \bar{u})^2 + \bar{w}^2} . \quad (24)$$

325 This ratio emphasizes more the downslope-upslope asymmetry than the criteria used in Lott (2016)  
 326 where only the downslope wind amplitude was measured in relation with the wind at the top of the  
 327 hill. The reason is that here the wind at the top of the hill is null so this measure makes little sense.  
 328 Here the ratio measures the upstream flow blocking as much as the downslope wind intensification  
 329 and we see that it can easily reach values around 4 or 5 for slopes near the boundary layer depth  
 330  $\delta(1) = 0.1$  and when  $J$  is sufficiently large. It always stays near 1 for small slopes and essentially  
 331 increases with  $J$  and  $S$  as expected.

## 332 5. Validation with a fully nonlinear model

333 To validate our results we now use the ocean general circulation model developed at MIT (MIT-  
 334 gcm) (Marshall et al., 1997) and which solves the fully nonlinear Boussinesq hydrostatic equations  
 335 on a cartesian mesh with a staggered Arakawa C-grid. We set the shape of the topography to a  
 336 Gaussian (Eq. 3) and take  $L = 1$  km and  $H = 150$  m which yield  $S = 0.15$ . Cells near the bottom  
 337 are cut with the partial cells strategy (Adcroft et al., 1997) with  $hFacmin = 0.1$  (if a fraction of  
 338 the cell is less than  $hFacMin$  then it is rounded to the nearer of 0 or  $hFacMin$ ). The total domain  
 339 horizontal size is 60 km with a stretched grid near the topography: the minimum and maximum  
 340 grid size are 60 m and 600 m respectively. We use a sponge layer at the lateral boundaries to relax

341 the dynamic variables (momentum and temperature) to the prescribed upstream profiles (2). The  
 342 relaxation time scale is 100 s in the innermost point of the sponge layer and 10 s in the outermost  
 343 point of the sponge layer. We also use a stretched grid in the vertical with maximum resolution  
 344 of 5.6 m at the topography and 415 m at the top of the domain. The total height of the domain is  
 345 50 km, and we use a sponge layer above 10 km with a relaxation time scale that varies quadrati-  
 346 cally with a minimum time scale of 10 s at the uppermost grid point (and infinite relaxation time  
 347 scale at 10 km). We use a constant wind shear ( $u_{0z} = 10^{-3} \text{ s}^{-1}$ ) and constant vertical temperature  
 348 gradient. The temperature is related to the density via a linear equation of state and we adjust  
 349 the vertical stratification  $N^2$  to match the non dimensional values of  $J$ : from  $N^2 = 5 \times 10^{-7} \text{ s}^{-2}$   
 350 ( $J = 0.5$ ) to  $N^2 = 1.6 \times 10^{-5} \text{ s}^{-2}$  ( $J = 16$ ). We use no-slip boundary conditions for momentum  
 351 at the topography and we set the bottom temperature to  $T = 0^\circ \text{ C}$  (we modified the code to get  
 352 a temperature flux at the boundary to ensure that the temperature at the topography is constant).  
 353 The horizontal and vertical viscosities for momentum are set to  $1 \text{ m}^2 \text{ s}^{-1}$ . The vertical and hori-  
 354 zontal coefficients of diffusivity for temperature are set to  $2 \text{ m}^2 \text{ s}^{-1}$ . We also added a horizontal  
 355 bi-harmonic damping with a coefficient of  $2 \times 10^3 \text{ m}^4 \text{ s}^{-1}$  for both the temperature and momentum  
 356 in order to damp grid scale noise generated at the topography. The time step is 0.5 s. The model  
 357 is integrated forward in time until we reach a steady state (usually less than one day).

358 The results for the vertical velocity field in Figs. 9a, 9b, and 9c, reproduce reasonably well the  
 359 corresponding predictions from the theory in Figs. 6d, Figs. 6e, and 6f respectively. The horizontal  
 360 scale and vertical variations are well reproduced, the amplitudes in the MITgcm are about 10%  
 361 smaller near  $\bar{z} = 1$  than in the theory, a difference we attribute to numerical dissipation that are not  
 362 easy to control. The results for the winds at low level in Figs. 9d, 9e, and 9f are also consistent  
 363 with those from the theory in Figs. 7d, Figs. 7e, and 7f respectively. The flow in the MITgcm  
 364 presents the upstream/downstream symmetry predicted by theory when  $J = 1$  Fig. 9a, and stronger  
 365 downslope than upslope winds when  $J = 9$  and  $J = 16$ . We conclude that there is a good agreement  
 366 between the global indexes defined in the theoretical model and the fully non-linear model (see  
 367 for instance the comparison of the emitted wave fluxes in Figs. 3a and 3b, or of the downslope  
 368 windstorm index in Fig. 8). The only noticeable difference is on the pressure drag in Fig. 2, the  
 369 MITgcm predicts a larger drag than in the theory. We have tried to understand the causes of the  
 370 differences, but find it difficult to correct the error. A reason is that the major differences between  
 371 the theory and the MITgcm are essentially located near the surface (not shown), i.e. at places  
 372 where viscous stress equals the Reynolds stress and where the stepwise treatment of the lower  
 373 boundary can produce grid-scale irregularities on these fields. As such irregularities are likely  
 374 to be damped out by dissipation as we move away from the surface, we can speculate that these

375 low level differences on the velocity shears and pressure are not significant in the context of the  
376 interactions between the waves and the large scale flow at upper levels.

## 377 **6. Conclusion**

378 In dynamical meteorology and oceanography, solutions with constant viscosity have always been  
379 a starting points to understand phenomena that involve the interaction between the surface and the  
380 boundary layer. Examples are numerous, from the Ekman et al. (1905) solutions systematically  
381 given in textbook, the Prandtl (1952) model for katabatic winds, the inclusion of a boundary  
382 layer in the Miles theory for the generation of oceanic waves (Benjamin, 1959), or in theories  
383 of sand ripples and dunes formation (Engelund, 1970) (see also Fowler (2001)). In waves and  
384 dune theories, the fact that the near surface wind profiles play a crucial role in the dynamics  
385 was early recognized (Miles, 1957; Benjamin, 1959) , and a first difficulty consisted in solving  
386 the fourth order Orr-Sommerfeld equation and to introduce a corrugated bottom at the surface  
387 (Fowler, 2001). A difficulty arises if one wishes to introduce stratification: the equation to solve  
388 becomes of the sixth order (see Eq. 17). This difficulty plus the facts that a constant eddy viscosity  
389 is a crude approximations of the turbulence in actual boundary layers, are two reasons why the  
390 viscous problem is not often treated in the stratified case. When it is, the techniques used are  
391 extremely involved (see for instance the introduction of "triple decks" in Sykes (1978)), and does  
392 not permit to derive uniform approximations of the solutions over the entire domain. As this  
393 last remark also holds for more sophisticated eddy viscosity closure, it is fair to say that theories  
394 failed so far in predicting the vertical profiles of the waves Reynolds stress, a quantity that is  
395 central in mountain meteorology. For these reasons but also because more and more papers in  
396 mountain meteorology call for a better understanding of the interaction between boundary layers  
397 and mountain waves, we found useful to solve the viscous mountain wave problem theoretically,  
398 and verify the theory with a fully nonlinear model (here the MITgcm). Note that in the context  
399 of stratified oceanic boundary layers over corrugate and tilted slopes, a recent paper by Passaggia  
400 et al. (2014) shares the same concern.

401 Once given this context, what are the messages that could be useful in a more realistic context?  
402 The first is probably that pressure drag and wave Reynolds stress are well predicted by inviscid  
403 theory and if we take for the incident flow, its value averaged over the inner layer depth. This depth  
404 has a definition that can be generalized, at least conceptually. For instance, if the boundary layer  
405 scheme uses first order closure with vertical diffusion coefficients, the coefficients and tendencies  
406 can be linearized around the large-scale resolved state. If we consider a small perturbation of  
407 given horizontal scale, the inner layer depth of interest is that where advection by the resolved  
408 wind equals the disturbance in boundary layer tendency. These predictions of the drag and waves

409 Reynolds stress remain valid until the mountain height equals the inner layer scale. Our theory  
410 does not go beyond that height. For higher mountains we should probably average the incident  
411 flow over the mountain height to obtain realistic predictions. Actually, this is what we find with  
412 our model when imposing free slip boundary condition in  $\bar{z} = \bar{h}$ , i.e. in an inviscid approximation  
413 where the boundary layer depth is drastically reduced (not shown).

414 For large values of the stratification, we also find that a good fraction of the stress is dissipated  
415 near the top of the inner layer, simply because the waves have shorter vertical wavelength and are  
416 more dissipated there. This effect is mitigated when the top of the hill is near the top of the inner  
417 layer scale again, but suggests that a good fraction of the mountain wave drag should be given  
418 back to the flow near the top of the inner layer. Another interesting result concerns the source of  
419 the mountain wave stress. When the mountain is well inside the inner layer, the wave stress is in  
420 good part extracted from the inner layer itself rather than from the solid earth as in the inviscid  
421 case. When the mountain slope approaches the inner layer depth this result is less applicable and  
422 a good part of the pseudo momentum flux is directed toward the surface as in the inviscid case  
423 (Durrán, 1995; Lott, 1998).

424 Our results could also be used to provide alternative views concerning the dynamics of upstream  
425 blocking and downslope winds. They occur through a near surface critical level dynamics and  
426 without upper level wave breaking (remember that our theory is linear inside the flow) providing  
427 that the flow is stable  $J > 1$ , and that the mountain slope is near the inner layer scale. This confirms  
428 the results in Lott (2016) and Damiens et al. (2018) who predicted these behaviors using simpler  
429 theories and using simulations with WRF including more sophisticated boundary layers. Another  
430 important result concern the structure of the inner layer itself: the downslope winds penetrate well  
431 into the inner it, as shows for instance Fig. 7 when  $J = 9$  or  $J = 16$ .

432 Last, for all the results presented here, we have neglected that the mountain gravity waves nec-  
433 essarily return to the surface in the constant shear case: they are all trapped, and this effect should  
434 be taken into account to give a more realistic treatment of the constant shear case. To take this into  
435 account within our theoretical framework we need to reject the hydrostatic approximation and we  
436 have to treat the inviscid solution in terms of Hankel functions (Keller, 1994), a solution we will  
437 describe in a future paper. Note that such subsequent development will also allow us to treat the  
438 non-stratified situation and describe the transition from the neutral to the stratified case. Here we  
439 wanted to treat the hydrostatic case first because an extremely rich dynamics already occur at low  
440 level and we do not need to attribute this dynamics to the fact that all the harmonics are trapped.

441 In this paper also, the background shear flow is constant, which corresponds to a boundary layer  
442 flow of infinite depth. Hence, even though we insist on using the terminology that the dynamics  
443 introduces an "inner" layer scale, it has to be clearly distinguished from the plausible presence



444 of a "boundary layer", where the incident wind present large curvature. Again, we can treat such  
 445 problem with our formalism by imposing background flow with non-zero curvature, a situation  
 446 that can introduced trapped lee waves in the non-hydrostatic case (Soufflet et al., 2019).

## 447 APPENDIX

### 448 A1. Pre-conditioning of the viscous solution

449 To evaluate  $\tilde{\mathbf{w}}_2$ ,  $\tilde{\mathbf{w}}_3$ , and  $\tilde{\mathbf{w}}_4$  we proceed as in Lott (2007), take the asymptotic forms in (18) when  
 450  $\tilde{z} > 5$  and integrate down to  $\tilde{z} = 0$  with a Runge-Kutta algorithm. Nevertheless these solutions are  
 451 ill-conditioned when it comes to the inversion of the boundary condition, essentially because  $\tilde{\mathbf{w}}_3$   
 452 and  $\tilde{\mathbf{w}}_4$  vary exponentially with altitude (see (18)). To circumvent this difficulty, rather than  $\tilde{\mathbf{w}}_2$ ,  
 453  $\tilde{\mathbf{w}}_3$ , and  $\tilde{\mathbf{w}}_4$  we have used 3 solutions  $\tilde{\mathbf{w}}_a$ ,  $\tilde{\mathbf{w}}_b$ , and  $\tilde{\mathbf{w}}_c$  which asymptotic behavior for  $\tilde{z} \rightarrow \infty$  all  
 454 match the inviscid solution  $\bar{\mathbf{w}}_I$  when  $\tilde{z} \rightarrow 0$ , but which do not grow exponentially fast when  $\tilde{z} \rightarrow 0$ :

$$455 \quad \tilde{\mathbf{w}}_a(\tilde{z}) = \tilde{\mathbf{w}}_2(\tilde{z}) + \tilde{a}_3\tilde{\mathbf{w}}_3(\tilde{z}) + \tilde{a}_4\tilde{\mathbf{w}}_4(\tilde{z}) \quad (\text{A1a})$$

$$456 \quad \tilde{\mathbf{w}}_b(\tilde{z}) = \tilde{\mathbf{w}}_2(\tilde{z}) + \tilde{b}_3\tilde{\mathbf{w}}_3(\tilde{z}) + \tilde{b}_4\tilde{\mathbf{w}}_4(\tilde{z}) \quad (\text{A1b})$$

$$457 \quad \tilde{\mathbf{w}}_c(\tilde{z}) = \tilde{\mathbf{w}}_2(\tilde{z}) + \tilde{c}_3(\bar{k})(\tilde{z}) + \tilde{c}_4\tilde{\mathbf{w}}_4(\tilde{z}). \quad (\text{A1c})$$

457 The three pairs  $(\tilde{a}_3, \tilde{a}_4)$ ,  $(\tilde{b}_3, \tilde{b}_4)$ ,  $(\tilde{c}_3, \tilde{c}_4)$  are then chosen so that  $(\partial_{\tilde{z}}\tilde{\mathbf{u}}_a(0), \partial_{\tilde{z}}\tilde{\mathbf{b}}_a(0)) = (0, 0)$ ,  
 458  $(\partial_{\tilde{z}}\tilde{\mathbf{u}}_b(0), \tilde{\mathbf{p}}_b(0)) = (0, 0)$ , and  $(\partial_{\tilde{z}}\tilde{\mathbf{b}}_c(0), \tilde{\mathbf{p}}_c(0)) = (0, 0)$  respectively. These three solutions are  
 459 shown in Fig. 10 for  $J = 1$  and  $Pr = 0.5$ , they show moderate variations with inner altitude  $\tilde{z}$ , the  
 460 exponential behavior of  $\tilde{\mathbf{w}}_3$  and  $\tilde{\mathbf{w}}_4$  has clearly been mitigated by adopting finite amplitudes values  
 461 for the variables and their derivatives at the surface. The boundary condition is then satisfied by  
 462 writing,

$$463 \quad \bar{w}(\bar{x}, \bar{h}) \approx \int_{-\infty}^{+\infty} \bar{k}\bar{\delta}(\bar{k}) (f_a(\bar{k})\tilde{\mathbf{w}}_a(\tilde{h}) + f_b(\bar{k})\tilde{\mathbf{w}}_b(\tilde{h}) + f_c(\bar{k})\tilde{\mathbf{w}}_c(\tilde{h})) e^{i\bar{k}\bar{x}} d\bar{k} = 0, \quad (\text{A2a})$$

$$464 \quad \bar{u}(\bar{x}, \bar{h}) \approx \int_{-\infty}^{+\infty} (f_a(\bar{k})\tilde{\mathbf{u}}_a(\tilde{h}) + f_b(\bar{k})\tilde{\mathbf{u}}_b(\tilde{h}) + f_c(\bar{k})\tilde{\mathbf{u}}_c(\tilde{h})) e^{i\bar{k}\bar{x}} d\bar{k} = -\bar{h}(\bar{x}), \quad (\text{A2b})$$

$$465 \quad \bar{b}(\bar{x}, \bar{h}) \approx \int_{-\infty}^{+\infty} (f_a(\bar{k})\tilde{\mathbf{b}}_a(\tilde{h}) + f_b(\bar{k})\tilde{\mathbf{b}}_b(\tilde{h}) + f_c(\bar{k})\tilde{\mathbf{b}}_c(\tilde{h})) e^{i\bar{k}\bar{x}} d\bar{k} = -J\bar{h}(\bar{x}), \quad (\text{A2c})$$

465 where  $\tilde{h}(\bar{x}, \bar{k}) = \bar{h}(\bar{x})/\bar{\delta}(\bar{k})$ . Once discretized in the horizontal and spectral domain, the set of  
 466 equations (20) corresponds to three linear equations involving nine matrices (for instance one of  
 467 the matrix has for components  $\bar{k}_j\bar{\delta}(\bar{k}_j)\tilde{\mathbf{w}}_a(\tilde{h}_{ij})e^{i\bar{k}_j\bar{x}_i}d\bar{k}$ ) and three unknown vectors (with compo-  
 468 nents  $f_a(\bar{k}_j)$ ,  $f_b(\bar{k}_j)$ , and  $f_c(\bar{k}_j)$ ) that can be inverted with conventional matrix inversion routines.

469 Still in this formalism, the uniform approximation of  $\bar{\mathbf{w}}$  in (19) writes,

$$\bar{\mathbf{w}}(\bar{k}, \bar{z}) = \bar{k}\bar{\delta}(k) \left[ f_a(\bar{k})\bar{\mathbf{w}}_a(\bar{k}, \bar{z}/\bar{\delta}(\bar{k})) + f_b(\bar{k})\bar{\mathbf{w}}_b(\bar{k}, \bar{z}/\bar{\delta}(\bar{k})) + f_c(\bar{k})\bar{\mathbf{w}}_c(\bar{k}, \bar{z}/\bar{\delta}(\bar{k})) \right] \quad (\text{A3})$$

470 again with similar expression for  $\bar{\mathbf{u}}$  and  $\bar{\mathbf{b}}$ .

## 471 A2. Numerical resolution

472 To solve numerically our problem we always take a domain of length  $\bar{X} = 100$  spanned by  $N =$   
473 1024 points, which corresponds to a spectral resolution around  $d\bar{k} \approx 0.01$  and a spatial resolution  
474 around  $d\bar{x} \approx 0.1$ . In the vertical we take grids of maximum depth  $\bar{Z} = 3$  and smoothly varying  
475 vertical resolution. The variable resolution is such that for  $\bar{z} > 10S$  the grid spacing  $dz \approx 0.03$   
476 whereas near around and below the mountain top  $dz \approx S/10$ . We will then systematically vary the  
477 other two non dimensional parameters of the problem  $S$ , and  $J$ .

478 Concerning the variations in slope  $S$ , we have to assume that the mountain is well in the boundary  
479 layer, a condition that needs to be satisfied for each harmonics. Although this pauses a theoretical  
480 problem since in the infinite Fourier integrals  $\bar{k}$  can become extremely large (and  $\bar{\delta}(\bar{k})$  very small)  
481 it can be handled numerically once fixed the horizontal scale of the domain over which Fourier  
482 series approximate Fourier transform and once fixed the number of horizontal grid points. More  
483 specifically, if  $\bar{k}_{max} = N\pi/X$ , the condition that the associated boundary layer depth is larger than  
484 the mountain top is  $\frac{S}{\bar{\delta}(\bar{k}_{max})} \approx 1$  or less. Nevertheless, and for moderately large domain length  $\bar{X}$  it  
485 happens that it is sufficient to satisfy this condition for the dominant wavenumbers, i.e. to satisfy  
486  $\frac{S}{\bar{\delta}(1)} \not\approx 1$ . This guaranties that the dominant harmonics forced by the obstacle are still well viscous  
487 near the mountain top. In this case, numerical convergence was found up to around  $S \approx 0.15$ .

## 488 Acknowledgement

489 This work was supported by the Laboratoire de Recherche Conventienn Yves Rocard, a collab-  
490 orative unit between CEA and Ecole Normale Supérieure.

## 491 References

- 492 Adcroft, A., C. Hill, and J. Marshall, 1997: Representation of topography by shaved  
493 cells in a height coordinate ocean model. *Mon. Wea. Rev.*, **125**, 2293–2315, doi:10.1175/  
494 1520-0493(1997)125<2293:ROTBSC>2.0.CO;2.
- 495 Ayotte, K., 2008: Computational modelling for wind energy assessment. *Journal of Wind Engi-  
496 neering and Industrial Aerodynamics*, 1571–1590, doi:10.1016/j.jweia.2008.02.002.
- 497 Baldwin, P., and P. H. Roberts, 1970: The critical layer in stratified shear flow. *Mathematika*, **17**,  
498 102–119.

- 499 Belcher, S. E., and N. Wood, 1996: Form and wave drag due to stably stratified turbulent flow over  
500 low ridges. *Quart. J. Roy. Meteor. Soc.*, **122**, 863–902.
- 501 Beljaars, A., J. Walmsley, and P. Taylor, 1987: A mixed spectral finite-difference model for neu-  
502 trally stratified boundary-layer flow over roughness changes and topography. *Boundary-Layer*  
503 *Meteorology*, **38 (3)**, 273–303.
- 504 Beljaars, A. C. M., A. R. Brown, and N. Wood, 2004: A new parametrization of turbulent oro-  
505 graphic form drag. *Quarterly Journal of the Royal Meteorological Society*, **130 (599)**, 1327–  
506 1347.
- 507 Benjamin, T. B., 1959: Shearing flow over a wavy boundary. *Journal of Fluid Mechanics*, **6 (2)**,  
508 161–205.
- 509 Booker, J. R., and F. P. Bretherton, 1967: The critical layer for internal gravity waves in a shear  
510 flow. *J. Fluid Mech.*, **27**, 102–109, doi:http://dx.doi.org/10.1017/S0022112067000515.
- 511 Charru, F., B. Andreotti, and P. Claudin, 2012: Sand ripples and dunes. *Annu. Rev. Fluid Mech.*,  
512 **45**, 469–493, doi:10.1146/annurev-fluid-011212-140806.
- 513 Damiens, F., F. Lott, C. Millet, and R. Plougonven, 2018: An adiabatic foehn effect. *Quart. J. Roy.*  
514 *Meteor. Soc.*, **144**, 1369–1381, doi:10.1002/qj.3272.
- 515 Doyle, J. D., and Coauthors, 2011: An intercomparison of t-rex mountain-wave simulations and  
516 implications for mesoscale predictability. *Monthly weather review*, **139 (9)**, 2811–2831.
- 517 Durran, D. R., 1990: Mountain waves and downslope winds. *AMS Meteorological Monographs*,  
518 **23**, 59–83.
- 519 Durran, D. R., 1995: Pseudomomentum diagnostics for two-dimensional stratified compressible  
520 flow. *Journal of the atmospheric sciences*, **52 (22)**, 3997–4009.
- 521 Ekman, V. W., and Coauthors, 1905: On the influence of the earth's rotation on ocean-currents.  
522 *Almqvist & Wiksells boktryckeri, A.-B.*,.
- 523 Eliassen, A., and E. Palm, 1961: On the transfer of energy in stationary mountain waves. *Geofys.*  
524 *Publ.*, **22**, 1–23.
- 525 Engelund, F., 1970: Instability of erodible beds. *Journal of Fluid Mechanics*, **42 (2)**, 225–244.
- 526 Fowler, A., 2001: Dunes and drumlins. *Geomorphological fluid mechanics*, Springer, 430–454.
- 527 Hazel, P., 1967: The effect of viscosity and heat conduction on internal gravity waves at a critical  
528 level. *Journal of Fluid Mechanics*, **30 (4)**, 775–783.

- 529 Hunt, J. C. R., S. Leibovich, and K. J. Richards, 1988: Turbulent shear flows over low hills. *Quart.*  
530 *J. Roy. Meteor. Soc.*, **114**, 1435–1470.
- 531 Jackson, P. S., and J. C. R. Hunt, 1975: Turbulent wind flow over low hill. *Quart. J. Roy. Meteor.*  
532 *Soc.*, **101**, 929–955.
- 533 Jiang, Q., J. D. Doyle, and R. B. Smith, 2006: Interaction between trapped waves and boundary  
534 layers. *J. Atmos. Sci.*, **63**, 617–633, doi:http://dx.doi.org/10.1175/JAS3640.1.
- 535 Keller, T. L., 1994: Implications of the hydrostatic assumption on atmospheric gravity waves.  
536 *Journal of the atmospheric sciences*, **51 (13)**, 1915–1929.
- 537 Lott, F., 1998: Linear mountain drag and averaged pseudo-momentum flux profiles in the presence  
538 of trapped lee waves. *Tellus A: Dynamic Meteorology and Oceanography*, **50 (1)**, 12–25.
- 539 Lott, F., 2007: The reflection of a stationary gravity wave by a viscous boundary layer. *J. Atmos.*  
540 *Sci.*, **139**, 3363–3371, doi:http://dx.doi.org/10.1175/JAS4020.1.
- 541 Lott, F., 2016: A new theory for downslope windstorms and trapped lee waves. *J. Atmos. Sci.*, **73**,  
542 3585–3597, doi:doi:10.1175/JAS-D-15-0342.1.
- 543 Lott, F., and M. Miller, 1997: A new subgrid scale orographic drag parameterization; its testing in  
544 the ecmwf model. *Quart. J. Roy. Meteor. Soc.*, **123**, 101–127.
- 545 Marshall, J., A. Adcroft, C. Hill, L. Perelman, and C. Heisey, 1997: A finite-volume, incompress-  
546 ible Navier Stokes model for studies of the ocean on parallel computers. *J. Geophys. Res.*, **102**,  
547 5753–5766, doi:10.1029/96JC02775.
- 548 Miles, J. W., 1957: On the generation of surface waves by shear flows. *Journal of Fluid Mechanics*,  
549 **3 (2)**, 185–204.
- 550 Olafsson, H., and P. Bougeault, 1997: The effect of rotation and surface friction on orographic  
551 drag. *J. Atmos. Sci.*, **54**, 193–210.
- 552 Passaggia, P.-Y., P. Meunier, and S. Le Dizes, 2014: Response of a stratified boundary layer on a  
553 tilted wall to surface undulations. *Journal of Fluid Mechanics*, **751**, 663684, doi:10.1017/jfm.  
554 2014.296.
- 555 Pithan, F., T. G. Shepherd, G. Zappa, and I. Sandu, 2016: Missing orographic drag leads to climate  
556 model biases in jet streams, blocking and storm tracks. *Geophysical Research Letters*, **43**, 7231–  
557 7240.
- 558 Prandtl, L., 1952: Essentials of fluid dynamics blackie. *London-Glasgow*, 452p.

- 559 Richard, E., P. Mascart, and E. C. Nickerson, 1989: The role of surface friction in downslope  
560 windstorms. *J. Appl. Meteor.*, **28**, 241–251.
- 561 Sandu, I., P. Bechtold, A. Beljaars, A. Bozzo, F. Pithan, T. Shepherd, and A. Zadra, 2015: Im-  
562 pacts of parameterized orographic drag on the northern hemisphere winter circulation, jour-  
563 nal of advances in modeling earth systems. *J. Adv. Model. Earth Syst.*, **8**, 196–211, doi:  
564 DOI:10.1002/2015MS000564.
- 565 Scinocca, J., and T. Shepherd, 1992: Nonlinear wave-activity conservation laws and hamilton-  
566 nian structure for the two-dimensional anelastic equations. *Journal of the atmospheric sciences*,  
567 **49 (1)**, 5–28.
- 568 Sheridan, P., S. Vosper, and P. Brown, 2017: Mountain waves in high resolution forecast models:  
569 Automated diagnostics of wave severity and impact on surface winds. *Atmosphere*, **8 (1)**, 24.
- 570 Sheridan, P. F., V. Horlacherxi, G. G. Rooney, P. Hignett, S. D. Mobbs, and S. Vosper, 2007:  
571 Influence of lee waves on the near surface flow downwind of the pennines. *Quart. J. Roy. Meteor.*  
572 *Soc.*, **133**, 1353–1369, doi:10.100a/2qj.110.
- 573 Smith, F., 1973: Laminar flow over a small hump on a flat plate. *Journal of Fluid Mechanics*,  
574 **57 (4)**, 803–824.
- 575 Smith, R. B., Q. Jiang, and J. D. Doyle, 2006: A theory of gravity wave absorption by a boundary  
576 layer. *J. Atmos. Sci.*, **63**, 774–781, doi:http://dx.doi.org/10.1175/JAS3631.1.
- 577 Smith, R. B., S. Skubis, J. D. Doyle, A. S. Broad, C. Kiemle, and H. Volkert, 2002: Mountain  
578 waves over the mont blanc: Influence of a stagnant boundary layer. *J. Atmos. Sci.*, **59**, 2073–  
579 2092.
- 580 Soufflet, C., F. Lott, and F. Damiens, 2019: Trapped mountain waves with critical level just below  
581 the surface. *Quart. J. Roy. Meteor. Soc.*, **Submitted**.
- 582 Sykes, R., 1978: Stratification effects in boundary layer flow over hills. *Proceedings of the Royal*  
583 *Society of London. A. Mathematical and Physical Sciences*, **361 (1705)**, 225–243.
- 584 Van Duin, C. A., and H. Kelder, 1986: Internal gravity waves in shear flows at large reynolds  
585 number. *Journal of Fluid Mechanics*, **169**, 293–306.
- 586 Wood, N., A. Brown, and F. Hewer, 2001: Parameterizing the effects of orography on the boundary  
587 layer: an alternative to effective roughness lengths. *Quart. J. Roy. Meteor. Soc.*, **127**, 759–777.
- 588 Wood, N., and P. Mason, 1993: The pressure force induced by neutral, turbulent flow over hills.  
589 *Quart. J. Roy. Meteor. Soc.*, **119**, 1233–1267.

590 **LIST OF FIGURES**

591 **Fig. 1.** Physical fields predicted by the theory in the hydrostatic case and when  $J = 4$ ,  $S = 0.01$ ,  
592  $\bar{\delta} = 0.1$ . a) Total wind vector  $(\bar{z} + \bar{u}, \bar{w})$ , b) vertical wind  $\bar{w}$ ; c) total stream function  $\bar{\psi}$  defined  
593 by:  $\partial_{\bar{z}}\bar{\psi} = \bar{z} + \bar{u}$ ; d) Vertical flux of action  $F^z$  (contour) and action flux vector  $(F^x, F^z)$ . In  
594 1b) and 1d) the negative values are dashed. . . . . 22

595 **Fig. 2.** Surface pressure drag predicted by theory and normalized by the amplitude of the invis-  
596 cid linear mountain gravity wave drag produced by a mountain of height  $H$  in a uniform  
597 flow of intensity  $U = u_0 \left( \frac{\delta(L^{-1})}{2} \right)$  and of stratification  $N: UNH^2$  (in non dimensional form:  
598  $\frac{\bar{\delta}(1)}{2} \sqrt{(J)S^2}$ , see Eq. 22). Grey dots are from the MITgcm with  $S = 0.15$ . . . . . 23

599 **Fig. 3.** a) Vertical profiles of the normalized wave Reynolds stress,  $\overline{u\bar{w}}$ , for  $S = 0.01$ . b) Pressure  
600 (black solid) and viscous (black dashed) stresses as defined on the RHS of Eq. (23). . . . . 24

601 **Fig. 4.** a) Normalized Reynolds stress emitted in the far field  $\overline{u\bar{w}}(\infty)$ ; b) Minimum value of  $\overline{u\bar{w}}(z)$   
602 for  $0 < \bar{z} < \infty$ . Grey dots are from the MITgcm with  $S = 0.15$ . . . . . 25

603 **Fig. 5.** Same as Fig. 1 for  $S = 0.15$ . . . . . 26

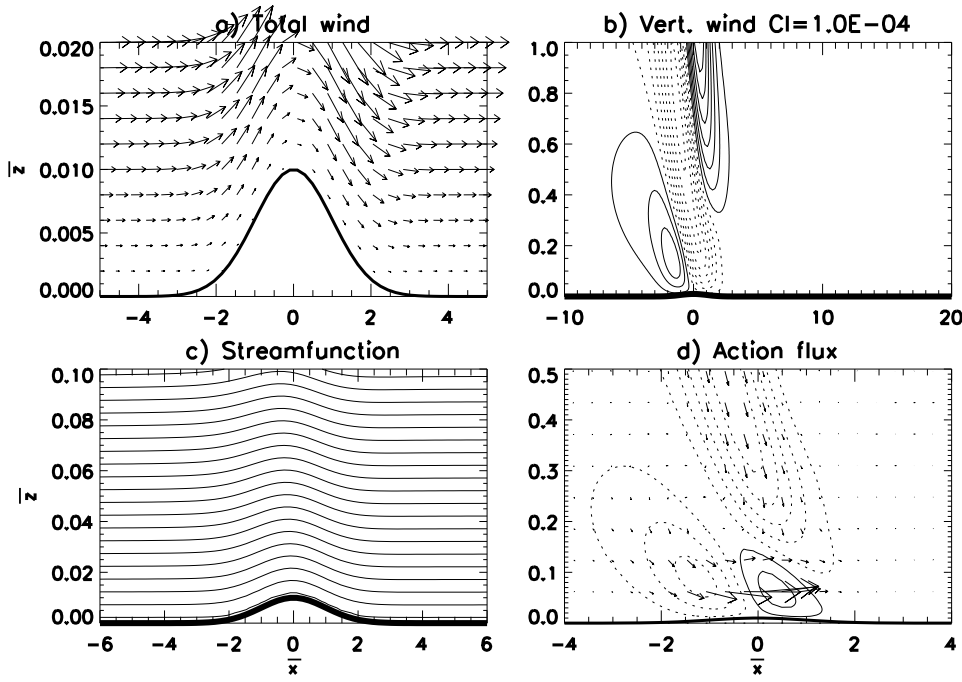
604 **Fig. 6.** Vertical velocity for different values of the Richardson number  $J$  and of the slope  $S$ . Bound-  
605 ary layer depth  $\delta(1) = 0.1$ . Contour intervals are shown in each panels. . . . . 27

606 **Fig. 7.** Wind vectors around the hill and for different values of the Richardson number  $J$  and of the  
607 slope  $S$ . Boundary layer depth  $\delta(1) = 0.1$ . . . . . 28

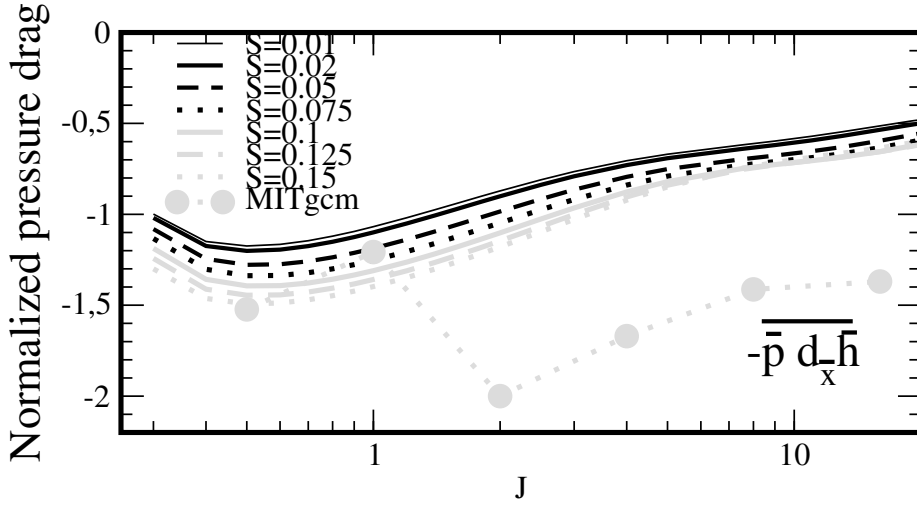
608 **Fig. 8.** Upstream blocking versus downslope windstorm index defined as the ratio between the max  
609 downslope wind amplitude and the max upslope wind amplitude. Grey dots are from the  
610 MITgcm with  $S = 0.15$ . . . . . 29

611 **Fig. 9.** Vertical velocities from the MITgcm in the upper panels correspond to the theory in  
612 Figs. 6d),6e) and 6f). Wind vectors from the MITgcm in the lower panels correspond to  
613 the theory in Figs. 7d),7e) and 7f). . . . . 30

614 **Fig. 10.** Uniform solutions  $U$  used to invert boundary conditions and to evaluate the wave fields over  
615 the entire domain.  $J = 1$ ,  $Pr = 0.5$ . All the solutions are expressed using inner variables. . . . . 31

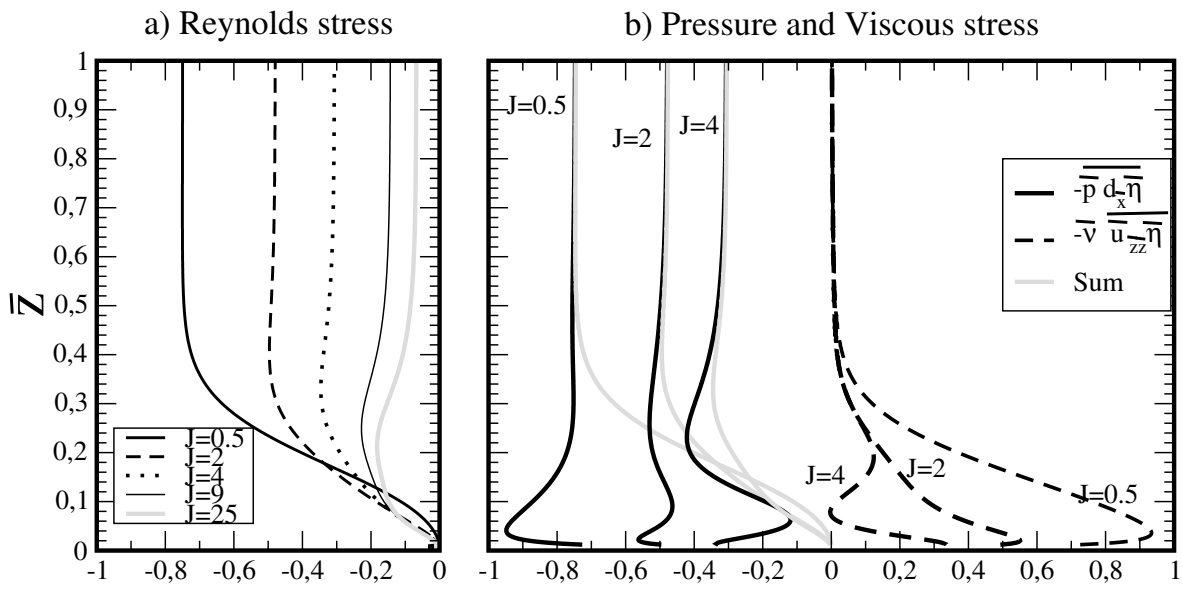


616 FIG. 1. Physical fields predicted by the theory in the hydrostatic case and when  $J = 4$ ,  $S = 0.01$ ,  $\bar{\delta} = 0.1$ . a)  
 617 Total wind vector  $(\bar{z} + \bar{u}, \bar{w})$ , b) vertical wind  $\bar{w}$ ; c) total streamfunction  $\bar{\psi}$  defined by:  $\partial_{\bar{z}}\bar{\psi} = \bar{z} + \bar{u}$ ; d) Vertical  
 618 flux of action  $F^z$  (contour) and action flux vector  $(F^x, F^z)$ . In 1b) and 1d) the negative values are dashed.

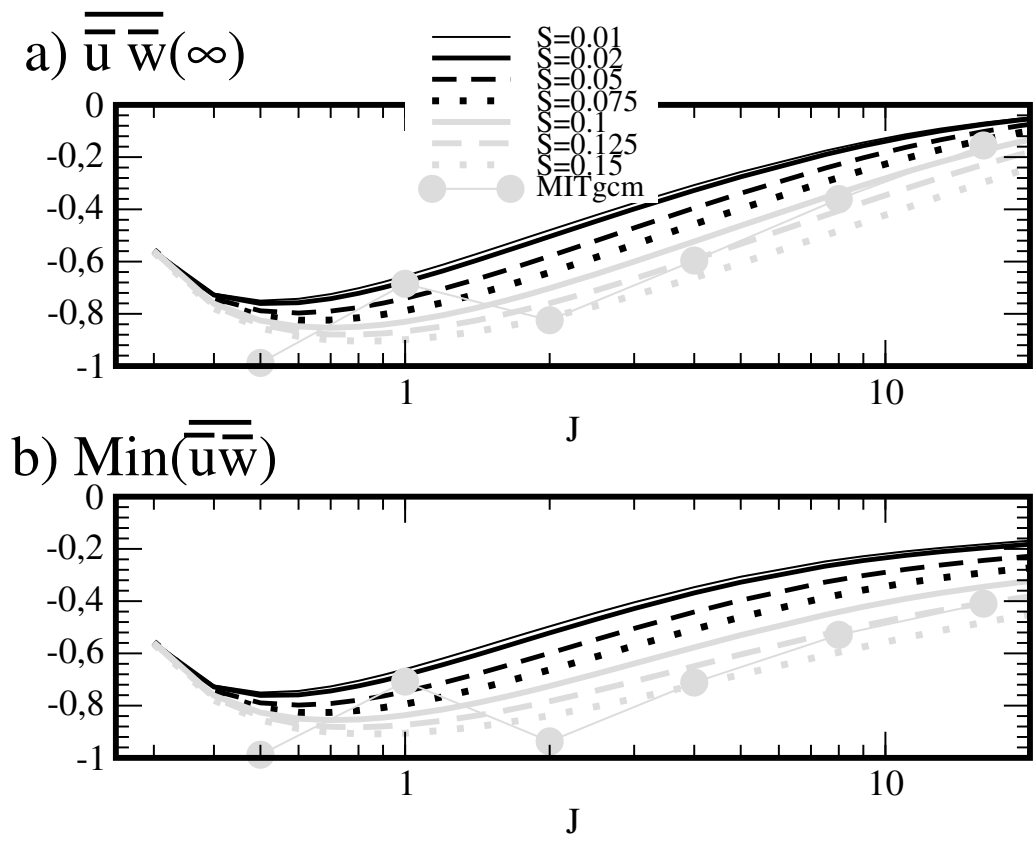


619 FIG. 2. Surface pressure drag predicted by theory and normalized by the amplitude of the inviscid linear  
 620 mountain gravity wave drag produced by a mountain of height  $H$  in a uniform flow of intensity  $U = u_0 \left( \frac{\delta(L^{-1})}{2} \right)$   
 621 and of stratification  $N: UNH^2$  (in non dimensional form:  $\frac{\bar{\delta}(1)}{2} \sqrt{J} S^2$ , see Eq. 22). Grey dots are from the  
 622 MITgcm with  $S = 0.15$ .





623 FIG. 3. a) Vertical profiles of the normalized wave Reynolds stress,  $\overline{\bar{u}\bar{w}}$ , for  $S = 0.01$ . b) Pressure (black  
 624 solid) and viscous (black dashed) stresses as defined on the RHS of Eq. (23).



625 FIG. 4. a) Normalized Reynolds stress emitted in the far field  $\overline{u'w'}(\infty)$ ; b) Minimum value of  $\overline{u'w'}(z)$  for  
 626  $0 < \bar{z} < \infty$ . Grey dots are from the MITgcm with  $S = 0.15$ .

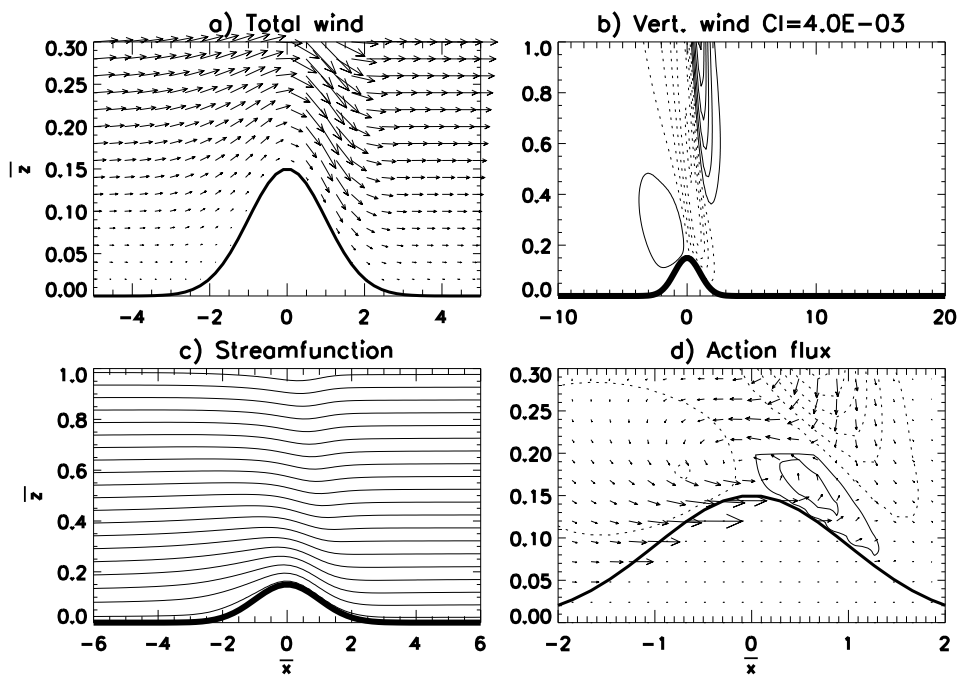
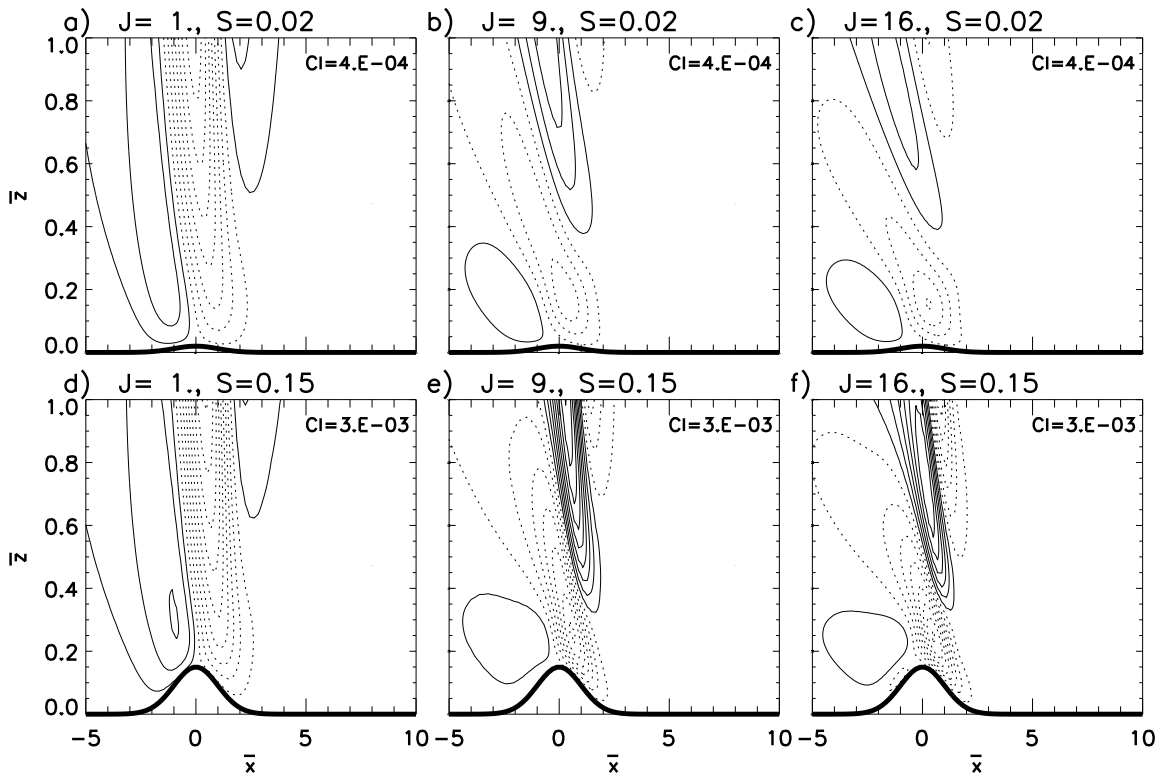
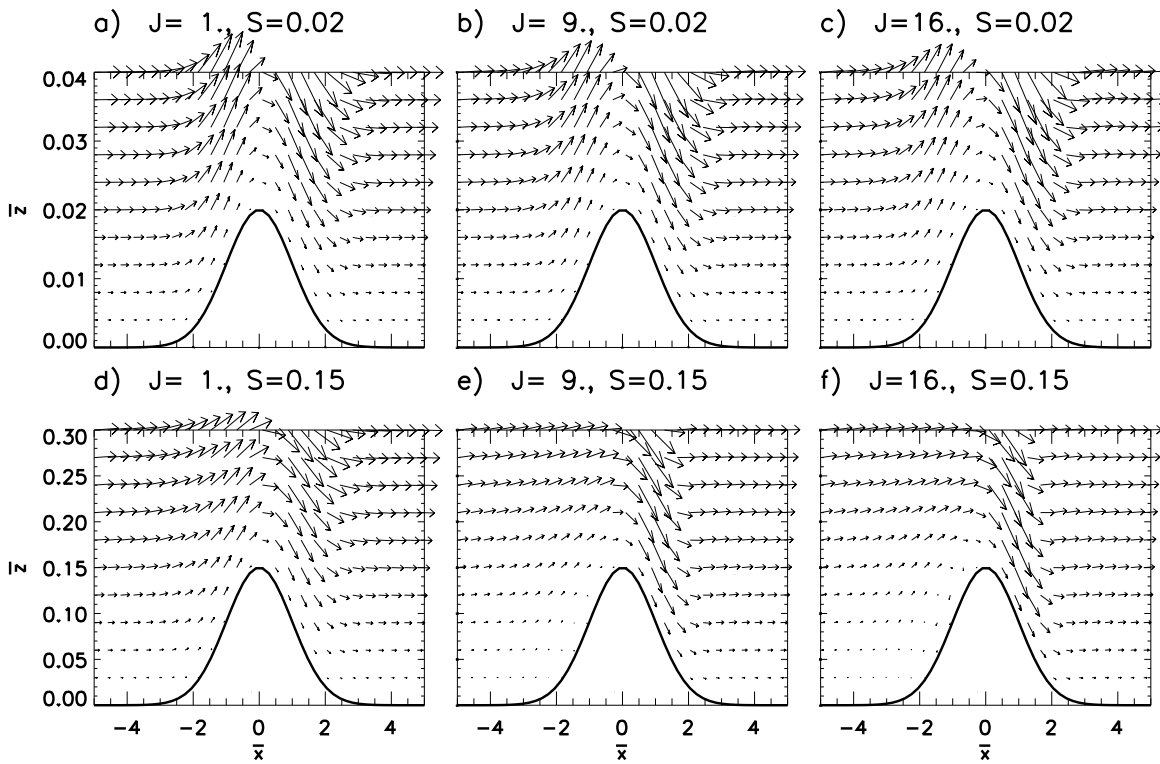


FIG. 5. Same as Fig. 1 for  $S = 0.15$ .

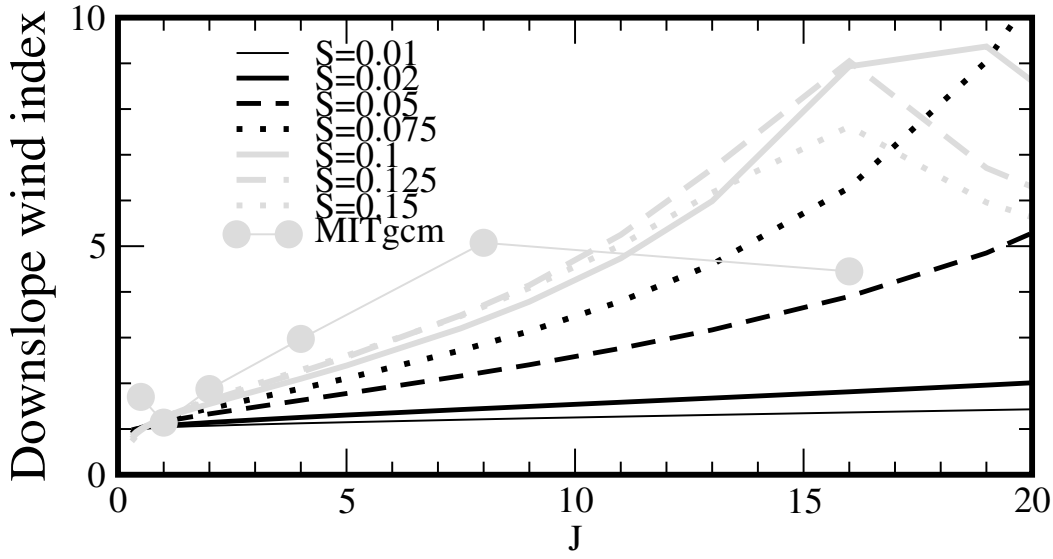


627 FIG. 6. Vertical velocity for different values of the Richardson number  $J$  and of the slope  $S$ . Boundary layer  
 628 depth  $\delta(1) = 0.1$ . Contour intervals are shown in each panels.

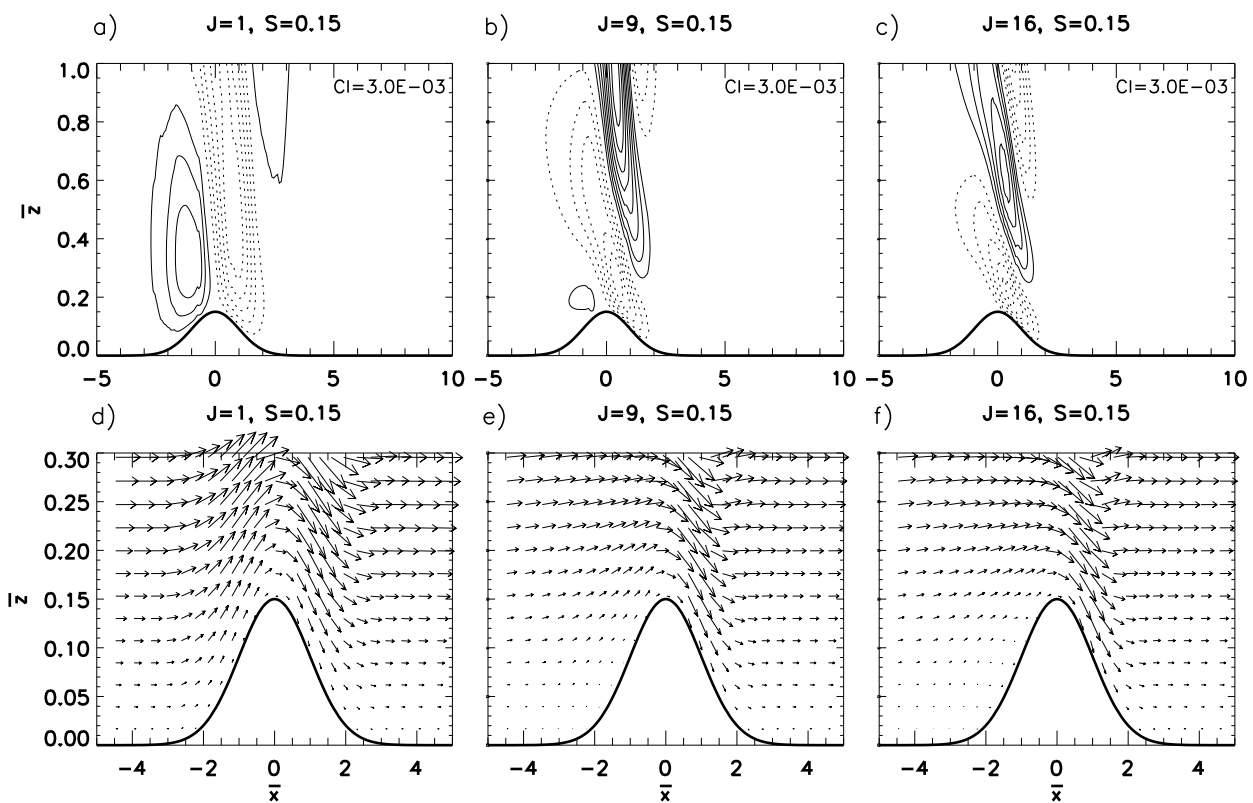


629 FIG. 7. Wind vectors around the hill and for different values of the Richardson number  $J$  and of the slope  $S$ .

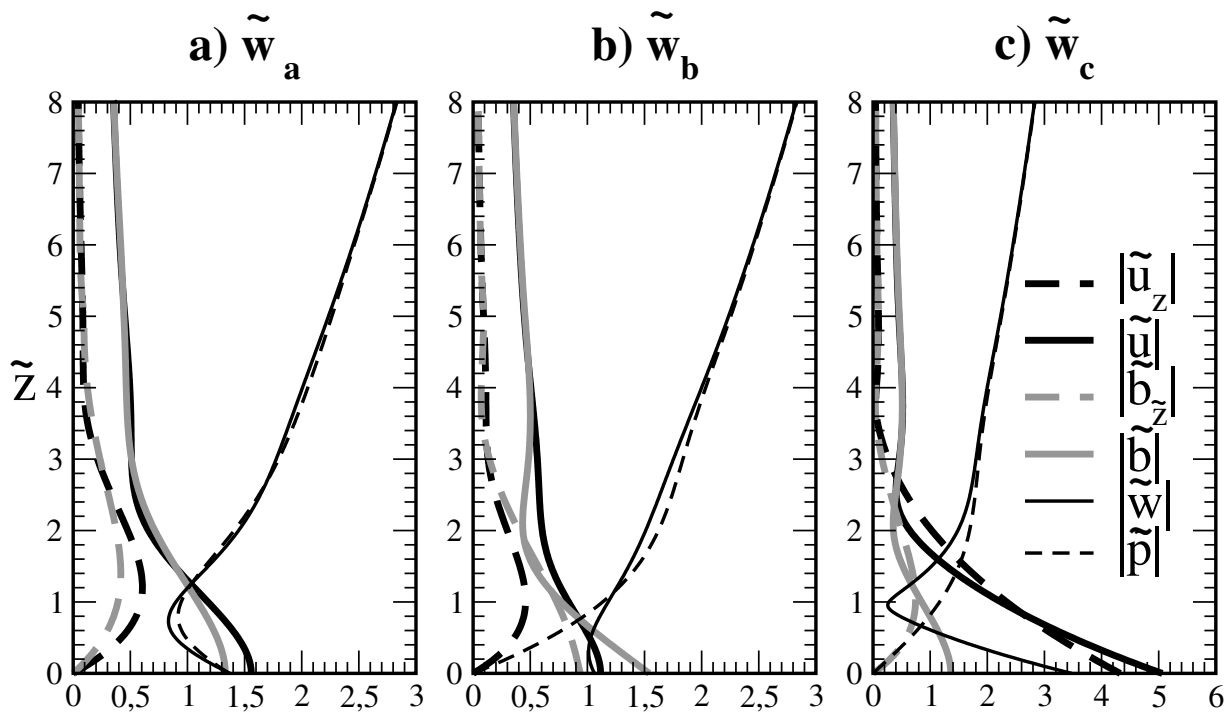
630 Boundary layer depth  $\delta(1) = 0.1$ .



631 FIG. 8. Upstream blocking versus downslope windstorm index defined as the ratio between the max downs-  
 632 slope wind amplitude and the max upslope wind amplitude. Grey dots are from the MITgcm with  $S = 0.15$ .



633 FIG. 9. Vertical velocities from the MITgcm in the upper panels correspond to the theory in Figs. 6d),6e) and  
 634 6f). Wind vectors from the MITgcm in the lower panels correspond to the theory in Figs. 7d),7e) and 7f).



635 FIG. 10. Uniform solutions used to invert boundary conditions and to evaluate the wave fields over the entire  
 636 domain.  $J = 1$ ,  $Pr = 0.5$ . All the solutions are expressed using inner variables.